Astronomy & Astrophysics

K2-106, a system containing a metal-rich planet and a planet of lower density[*],[**]

E. W. Guenther[1,7], O. Barragán[2], F. Dai[3], D. Gandolfi[2], T. Hirano[4], M. Fridlund[5,6,7], L. Fossati[8], A. Chau[9], R. Helled[9], J. Korth[10], J. Prieto-Arranz[7,11], D. Nespral[7,11], G. Antoniciello[2], H. Deeg[7,11], M. Hjorth[12], S. Grziwa[10], S. Albrecht[12], A. P. Hatzes[1], H. Rauer[13,14], Sz. Csizmadia[13], A. M. S. Smith[13], J. Cabrera[13], N. Narita[15,16,17], P. Arriagada[18], J. Burt[3], R. P. Butler[18], W. D. Cochran[19], J. D. Crane[20], Ph. Eigmüller[13], A. Erikson[13], J. A. Johnson[21], A. Kiilerich[12], D. Kubyshkina[8], E. Palle[7,11], C. M. Persson[6], M. Pätzold[10], S. Sabotta[1], B. Sato[4], St. A. Shectman[20], J. K. Teske[18,20], I. B. Thompson[20], V. Van Eylen[5], G. Nowak[7,11], A. Vanderburg[21], J. N. Winn[22], and R. A. Wittenmyer[23]

(Affiliations can be found after the references)

ABSTRACT

Aims. Planets in the mass range from 2 to 15 $M_\oplus$ are very diverse. Some of them have low densities, while others are very dense. By measuring the masses and radii, the mean densities, structure, and composition of the planets are constrained. These parameters also give us important information about their formation and evolution, and about possible processes for atmospheric loss.

Methods. We determined the masses, radii, and mean densities for the two transiting planets orbiting K2-106. The inner planet has an ultra-short period of 0.57 days. The period of the outer planet is 13.3 days.

Results. Although the two planets have similar masses, their densities are very different. For K2-106b we derive $M_b = 8.36^{+0.96}_{-0.94}$ $M_\oplus$, $R_b = 1.52 \pm 0.16\,R_\oplus$, and a high density of $13.1^{+5.4}_{-3.6}$ g cm^{-3}. For K2-106c, we find $M_c = 5.8^{+3.3}_{-3.0}$ $M_\oplus$, $R_c = 2.50^{+0.27}_{-0.26}$ $R_\oplus$ and a relatively low density of $2.0^{+1.6}_{-1.1}$ g cm^{-3}.

Conclusions. Since the system contains two planets of almost the same mass, but different distances from the host star, it is an excellent laboratory to study atmospheric escape. In agreement with the theory of atmospheric-loss processes, it is likely that the outer planet has a hydrogen-dominated atmosphere. The mass and radius of the inner planet is in agreement with theoretical models predicting an iron core containing 80^{+20}_{-30}% of its mass. Such a high metal content is surprising, particularly given that the star has an ordinary (solar) metal abundance. We discuss various possible formation scenarios for this unusual planet.

Key words. techniques: photometric – techniques: radial velocities – stars: abundances – stars: individual: TYC 608-458-1 – planetary systems

1. Introduction

In recent years, many planets with masses lower than 15 $M_\oplus$ have been discovered. Surprisingly, these planets show a great diversity in bulk densities (see, for example, Hatzes & Rauer 2015). It is obvious that the planets with the highest densities must be rocky, while those with the lowest densities must have a large fraction of volatiles such as hydrogen. Planets of intermediate densities could in principle have many different compositions, but there is now growing evidence that they also have rocky cores and less extended hydrogen atmospheres (see, for example, Chen et al. 2017). A picture has thus emerged in which the diversity of low-mass exoplanets is explained by the different size of the hydrogen atmospheres – some planets have very extended atmospheres, some have less extended ones, and others do not have them at all.

Why do some planets have hydrogen atmospheres and others do not? A crucial element for solving this problem was the result that low-mass close-in planets ($a \leq 0.05$ AU) tend to have high bulk densities. It is thus unlikely that they have extended hydrogen atmospheres. These planets are CoRoT-7b (Léger et al. 2009), Kepler-10b (Batalha et al. 2011), Kepler-36b (Carter et al. 2012), Kepler-78b (Sanchis-Ojeda et al. 2013), Kepler-93b (Dressing et al. 2015), HD 219134b (Motalebi et al. 2015), GJ 1132b, (Berta-Thompson et al. 2015), WASP-47e (Dai et al. 2015; Sinukoff et al. 2017a), and HD3167b (Gandolfi et al. 2017).

This collection of findings led to the hypothesis that atmospheric escape must play an important role in the formation and evolution of planets (e.g., Lammer et al. 2014; Sanchis-Ojeda et al. 2014; Lundkvist et al. 2016; Cubillos et al. 2017). For example, Cubillos et al. (2017) showed that planets with restricted Jeans escape parameters $\Lambda \leq 20$ cannot retain hydrogen-dominated atmospheres. The restricted Jeans escape parameter is defined as $\Lambda = \frac{GM_{pl}m_H}{k_B T_{eq} R_{pl}}$ (Fossati et al. 2017; see also the description in Cubillos et al. 2017).

The atmospheres of planets with Λ values lower than 20−40, depending on the system parameters, lie in the "boil-off" regime (Owen & Wu 2016; Cubillos et al. 2017), where the escape is

driven by the atmospheric thermal energy and low planetary gravity, rather than the high-energy (XUV) stellar flux. Atmospheric escape can thereby explain why low-mass close-in planets do not have extended hydrogen atmospheres.

The atmospheric escape rates have been determined for a number of planets with $M > 15\ M_\oplus$ by analyzing the profiles of the Lyman-α lines. For example, Bourrier et al. (2016) derived an escape rate of $\sim 2.5 \times 10^8$ g s^{-1} for GJ 436 b. This system is of particular interest for atmospheric escape studies because of the large hydrogen corona that has been detected around the planet (Ehrenreich et al. 2015). These results clearly support the idea that atmospheric loss processes are an important factor in the evolution of low-mass planets. Because the escape rate depends on the amount of XUV-radiation that a planet receives during its lifetime, as well as on its mass, it would be ideal to study a system that has two transiting planets of the same mass but at different distances from the host star.

Finding such a system and deriving the masses and radii of the planets is thus important. Density measurements of planets are not only important to study atmospheric escape, but also to constrain the structure of exoplanets, which in turn gives us important clues as to where and how they formed (Raymond et al. 2013). In this article, we point out that K2-106 is such a system.

Recently, Adams et al. (2017) found that the star K2-106 (EPIC 220674823, TYC 608-458-1) has two transiting planets. The inner planet has an ultra-short period of $P = 0.571308 \pm 0.00003$ d (ultra-short period planets have orbital periods shorter than one day). Adams et al. (2017) derived a radius of $R_{\rm p} = 1.46 \pm 0.14\ R_\oplus$. For the outer planet, these authors derived an orbital period of $P = 13.341245 \pm 0.0001$ d, and a radius of $R_{\rm p} = 2.53 \pm 0.14\ R_\oplus$. This system is particularly interesting because it hosts an ultra-short period planet that is subject to strong stellar irradiation and an outer planet at a relatively large distance from the host star, where the atmospheric escape rate is expected to be much lower. Within the framework of the KESPRINT collaboration, we re-derive the stellar fundamental parameters and determine masses, radii, and densities of the two planets[1]. We show that the two planets have similar masses and not very different densities. They are thus particularly interesting for learning more about the formation and evolution of planets.

2. Radial velocity measurements

We obtained absolute and relative radial velocities (RVs) using five different instruments. The relative RVs were obtained with HDS, PFS, and FIES and are described in Sect. 2.1 (results are listed in Table 1). The absolute RVs were obtained with HARPS and HARPS-N, and are described in Sect. 2.2 (results are listed in Table 2).

2.1. HDS, PFS, and FIES

PFS: between August 14, 2016, and January 14, 2017, we obtained 13 spectra of K2-106 with the Carnegie Planet Finder Spectrograph (PFS) (Crane et al. 2006, 2008, 2010). PFS is an échelle spectrograph on the 6.5 m *Magellan/Clay* Telescope at Las Campanas Observatory in Chile. It employs an iodine gas cell to superimpose well-characterized absorption features onto the stellar spectrum. The iodine absorption lines are used to

---

[1] This paper continues a series of papers on K2 planet investigations that were previously published by two collaborations, ESPRINT and KEST, which have recently merged to form the KESPRINT collaboration (see, e.g., Narita et al. 2017; Eigmüller et al. 2017).

Table 1. RV measurements of K2-106 obtained with PFS[1], HDS[2], and FIES[3].

$BJD_{\rm TDB}$[4] $-2\,450\,000$	RV[5] [km s^{-1}]	$\pm\sigma$ [km s^{-1}]	Instrument
7614.81876	0.0055	0.002	PFS
7615.82964	0.0001	0.002	PFS
7616.82147	−0.0012	0.003	PFS
7617.83381	0.0155	0.003	PFS
7618.76739	−0.0038	0.002	PFS
7621.83249	0.0006	0.002	PFS
7623.75032	−0.0043	0.003	PFS
7624.73484	−0.0151	0.005	PFS
7760.54699	0.0000	0.003	PFS
7763.55780	0.0035	0.003	PFS
7764.55645	0.0144	0.004	PFS
7765.55324	−0.0038	0.004	PFS
7767.55174	0.0031	0.004	PFS
7673.98378	−0.0095	0.005	HDS
7675.04835	0.0078	0.005	HDS
7676.01717	0.0078	0.005	HDS
7666.65017	0.0016	0.0050	FIES
7668.56785	0.0163	0.0043	FIES
7669.50586	0.0068	0.0036	FIES
7683.46006	0.0144	0.0068	FIES
7684.59951	0.0206	0.0061	FIES
7717.51153	−0.0002	0.0045	FIES

Notes. [1] RV offset for PFS: $1.2^{+1.5}_{-1.5}$ m s^{-1}, jitter term $3.9^{+1.7}_{-1.3}$ m s^{-1}. [2] RV offset for HDS: $2.0^{+8.7}_{-8.3}$ m s^{-1}, jitter term $10.8^{+28.7}_{-7.6}$ m s^{-1}. [3] RV offset for FIES: $10.2^{+2.4}_{-2.4}$ m s^{-1}, jitter term $2.3^{+3.0}_{-1.6}$ m s^{-1}. RV offset for HIRES: $-2.09^{+0.91}_{-0.93}$ m s^{-1}, jitter term $5.0^{+0.8}_{-0.7}$ m s^{-1}. [4] Barycentric Julian dates are given in barycentric dynamical time. [5] Relative RV.

establish the wavelength scale and instrumental profile (Crane et al. 2010). The detector was read out in the standard 2×2 binned mode. Exposure times ranged from 20−40 min, giving a signal-to-noise ratio (S/N) of 50−140 pixel^{-1} and a resolution of $\lambda/\Delta\lambda \sim 76\,000$ in the wavelength range of the iodine absorption lines. An additional iodine-free spectrum with higher resolution and higher S/N was obtained to serve as a template spectrum for the Doppler analysis. The relative RVs were extracted from the spectrum using the techniques described by Butler et al. (1996). The internal measurement uncertainties (ranging from 2−4 m s^{-1}) were determined from the scatter in the derived RVs based on individual 2 Å chunks of the spectrum (Butler et al. 1996). Since the spectral lines of the I$_2$-cell are superposed on the stellar spectrum, spectra taken with the I$_2$-cell were not used to determine the bisectors (see below in Sect. 2.2).

HDS: we obtained three RV measurements of K2-106 with the High Dispersion Spectrograph (HDS; Noguchi et al. 2002) on the 8.2 m Subaru Telescope. The spectra were obtained from October 12 to 14, 2016. We used image slicer 2 (Tajitsu et al. 2012), achieving a spectral resolution of $\lambda/\Delta\lambda \sim 85\,000$ and a typical S/N of 70−80 per pixel close to the sodium D lines. This instrument is also equipped with an I$_2$ cell (see Sato et al. 2002, for the HDS RV analysis). As with the PFS, the RVs are measured relative to a template spectrum taken by the same instrument without the I$_2$-cell.

FIES: we also obtained six RV measurements with the FIbre-fed Echelle Spectrograph (FIES; Frandsen & Lindberg 1999; Telting et al. 2014) on the 2.56 m Nordic Optical Telescope (NOT) at the Observatorio del Roque de los Muchachos,

Table 2. RV measurements K2-106 obtained with HARPS-N[1] and HARPS[2].

BJD$_{TDB}$ $-2\,450\,000$[3]	RV[4] [km s^{-1}]	$\pm\sigma$ [km s^{-1}]	Instrument	$FWHM$ [km s^{-1}]	BIS [km s^{-1}]	Ca II-S-index	$\log R'_{HK}$	S/N
7692.379446	−15.7430	0.0034	HARPS-N	6.82659	−0.045	0.164 ± 0.013	−4.94 ± 0.08	27.3 ± 1.2
7692.449096	−15.7332	0.0028	HARPS-N	6.82738	−0.046	0.166 ± 0.010	−4.93 ± 0.06	31.6 ± 1.1
7692.530008	−15.7332	0.0031	HARPS-N	6.83729	−0.049	0.159 ± 0.011	−4.97 ± 0.07	30.8 ± 1.1
7692.602841	−15.7323	0.0017	HARPS-N	6.83159	−0.044	0.154 ± 0.005	−5.01 ± 0.04	49.0 ± 1.5
7693.372417	−15.7358	0.0020	HARPS-N	6.82553	−0.027	0.138 ± 0.011	−5.14 ± 0.10	32.7 ± 1.2
7693.458907	−15.7400	0.0040	HARPS-N	6.84200	−0.037	0.154 ± 0.016	−5.01 ± 0.11	25.8 ± 1.1
7693.526485	−15.7428	0.0033	HARPS-N	6.82186	−0.034	0.169 ± 0.013	−4.91 ± 0.07	29.4 ± 1.1
7693.623125	−15.7309	0.0040	HARPS-N	6.82752	−0.019	0.194 ± 0.017	−4.79 ± 0.07	25.9 ± 1.8
7694.378314	−15.7309	0.0027	HARPS-N	6.81469	−0.040	0.146 ± 0.009	−5.07 ± 0.08	33.2 ± 1.2
7694.463901	−15.7341	0.0033	HARPS-N	6.83332	−0.052	0.150 ± 0.012	−5.04 ± 0.09	29.0 ± 1.0
7694.532289	−15.7372	0.0025	HARPS-N	6.81328	−0.047	0.147 ± 0.008	−5.06 ± 0.07	35.4 ± 1.1
7782.372461	−15.7278	0.0032	HARPS-N	6.83734	−0.037	0.148 ± 0.011	−5.05 ± 0.09	31.4 ± 1.7
7686.681371	−15.7431	0.0046	HARPS	6.88550	−0.019908	0.144 ± 0.023	−5.09 ± 0.19	23.1 ± 1.3
7688.599844	−15.7245	0.0032	HARPS	6.89222	−0.044137	0.151 ± 0.014	−5.03 ± 0.11	31.0 ± 1.4
7689.614348	−15.7419	0.0030	HARPS	6.89334	−0.024879	0.123 ± 0.013	−5.32 ± 0.19	32.4 ± 1.3
7689.664034	−15.7353	0.0024	HARPS	6.90754	−0.031006	0.172 ± 0.010	−4.90 ± 0.06	38.6 ± 1.3
7690.634880	−15.7407	0.0032	HARPS	6.89677	−0.026417	0.146 ± 0.016	−5.07 ± 0.13	30.9 ± 1.3
7690.707945	−15.7422	0.0031	HARPS	6.91026	−0.032698	0.187 ± 0.015	−4.87 ± 0.08	32.2 ± 1.4
7691.580784	−15.7225	0.0024	HARPS	6.89344	−0.034861	0.134 ± 0.010	−5.18 ± 0.10	38.9 ± 1.4
7691.694275	−15.7339	0.0027	HARPS	6.90384	−0.034266	0.118 ± 0.013	−5.60 ± 0.35	36.1 ± 1.4
7694.633396	−15.7395	0.0033	HARPS	6.91074	−0.027830	0.230 ± 0.016	−4.66 ± 0.05	30.5 ± 1.3
7694.707919	−15.7359	0.0035	HARPS	6.90179	−0.007927	0.126 ± 0.018	−5.43 ± 0.34	29.5 ± 1.5
7695.599038	−15.7294	0.0044	HARPS	6.91306	−0.036791	0.184 ± 0.020	−4.84 ± 0.10	24.2 ± 1.3
7695.682507	−15.7343	0.0042	HARPS	6.93653	−0.016037	0.198 ± 0.020	−4.82 ± 0.09	25.3 ± 1.4
7696.568244	−15.7246	0.0034	HARPS	6.90287	−0.035173	0.081 ± 0.015	[6]	29.1 ± 1.4
7696.642708	−15.7293	0.0029	HARPS	6.88997	−0.035394	0.158 ± 0.013	−5.05 ± 0.10	33.9 ± 1.3
7697.588441	−15.7326	0.0035	HARPS	6.90341	−0.024429	0.141 ± 0.017	−5.11 ± 0.15	29.0 ± 1.3
7697.670196	−15.7336	0.0030	HARPS	6.90300	−0.033715	0.131 ± 0.015	−5.21 ± 0.17	32.9 ± 1.4
7717.539931	−15.7363	0.0036	HARPS	6.90771	−0.008729	0.177 ± 0.016	−4.93 ± 0.10	27.6 ± 1.3
7717.609347[5]	−15.7502	0.0056	HARPS	6.88414	—0.036983	0.202 ± 0.034	−4.76 ± 0.14	20.3 ± 1.4
7719.534214	−15.7280	0.0028	HARPS	6.90219	−0.032777	0.131 ± 0.014	−5.22 ± 0.16	34.4 ± 1.3
7719.601212	−15.7235	0.0033	HARPS	6.90281	−0.042827	0.165 ± 0.017	−4.94 ± 0.10	30.8 ± 1.3

Notes. [1] Systemic RV of HARPS-N: $-15\,735.77^{+1.20}_{-1.18}$ m s^{-1}, jitter term $1.9^{+1.5}_{-1.2}$ m s^{-1}. [2] Systemic RV of HARPS: $-15\,732.70^{+0.90}_{-0.92}$ m s^{-1}, jitter term $4.9^{+0.76}_{-0.65}$ m s^{-1}. [3] Barycentric Julian dates are given in barycentric dynamical time. [4] Absolute RV. [5] Spectrum with very low S/N, not used for the fit. [6] Value could not be obtained.

La Palma (Spain). The observations were carried out from October 5 to November 25, 2016, as part of the observing programs 54-205, 54-027, and 54-211. We used the 1.3″ high-resolution fiber ($\lambda/\Delta\lambda$ 67 000) and set the exposure time to 2700 s, following the same observing strategy as Gandolfi et al. (2015). We traced the RV drift of the instrument by acquiring ThAr spectra with long exposures ($T_{\exp} \approx 35$ s) immediately before and after each observation. The data were reduced using standard IRAF and IDL routines. The S/N of the extracted spectra is about 35 per pixel at 5500 Å. RVs were derived via multi-order cross correlations, using the stellar spectrum with the highest S/N as template.

HIRES RV measurements from the literature: while this article was being refereed, we learned that another group had also undertaken RV measurements of K2-106 and uploaded their article on the preprint server (Sinukoff et al. 2017b). Their work included 35 relative RV measurements obtained with Keck-HIRES, which we also included in our analysis.

2.2. HARPS-N and HARPS

We obtained 12 RV measurements with the HARPS-N spectrograph (Cosentino et al. 2012) on the 3.58 m Telescopio

Nazionale *Galileo* (TNG) at La Palma in programs CAT16B-61, A34TAC_10, A34TAC_44, and 20 RVs with the HARPS spectrograph (Mayor 2003) on the 3.6 m ESO telescope at La Silla in program 098.C-0860. The HARPS-N spectra were obtained from October 30, 2016 to January 28, 2017, and the HARPS spectra from October 25 to November 27, 2016. Both spectrographs have a resolving power $\lambda/\Delta\lambda \sim 115\,000$. HARPS-N covers the wavelength region from 3780 Å to 6910 Å, and HARPS from 3830 Å to 6900 Å. All calibration frames were taken using the standard procedures for these instruments. The spectra were reduced and extracted using the dedicated HARPS/HARPS-N pipelines. The RVs were determined by using a cross-correlation method with a numerical mask that corresponds to a G2 star (Baranne et al. 1996; Pepe et al. 2002). The RV measurements were obtained by fitting a Gaussian function to the average cross-correlation function (CCF). The data reduction pipelines for both instruments also provide the absolute RV, and the bisector span. Because of the high resolution of the HARPS spectrographs, these spectra are particularly useful for the bisector analysis. We extracted the S-index and $\log R'_{HK}$ activity indicators from the HARPS and HARPS-N spectra. The measurements obtained with HARPS-N, and HARPS are listed in Table 2.

Table 3. Properties of the host star.

	Adams et al. (2017)	*Gaia* and $T_{\rm eff}$	This work[1]
$M_*[M_\odot]$	0.93 ± 0.01	0.902 ± 0.027[2]	0.945 ± 0.063
$R_*[R_\odot]$	0.83 ± 0.04	0.882 ± 0.050[2]	0.869 ± 0.088
$T_{\rm eff}$ [K]	5590 ± 51	...	5470 ± 30
$\log(g)$	4.56 ± 0.09	4.474 ± 0.053[2]	4.53 ± 0.08
[Fe/H]	0.025 ± 0.020		-0.025 ± 0.05
[Si/H]	...	...	-0.05 ± 0.05
[Ca/H]	...	...	$+0.08 \pm 0.05$
[Ni/H]	...	...	-0.02 ± 0.05
[Na/H]	...	...	$+0.05 \pm 0.05$
$v \sin i$ [km s^{-1}]	...	...	2.8 ± 0.35
$v_{\rm macro}$ [km s^{-1}]	...	...	1.7 ± 0.35
$v_{\rm micro}$ [km s^{-1}]	...	...	0.9 ± 0.1[3]
$A_{\rm v}$ [mag]	...	...	0.1 ± 0.1
distance [pc]	...	253 ± 50	...

Notes. [1] Spectroscopic determination as derived from the HARPS and HARPS-N spectra. [2] Derived using $T_{\rm eff}$, [Fe/H] from HARPS and HARPS-N, and the *Gaia* parallax in Sect. 3.1. [3] Using the empirical formula from Bruntt et al. (2010).

3. Combined analysis and properties of the host star and the planets

3.1. Properties of the host star

K2-106 (EPIC 220674823, TYC 608-458-1) is a G5V star with $V = 12.10$, located at RA: 00$^{\rm h}$52$^{\rm m}$19.147$^{\rm s}$, Dec: $+10°47'40.92''$ ($l = 123.2840°$, $b = -52.0764°$). The photospheric parameters, that is, effective temperature $T_{\rm eff}$, surface gravity $\log(g)$, metal content [M/H], and projected rotation velocity $v \sin i$, were determined spectroscopically by Adams et al. (2017) along with the stellar mass and radius. The authors used three spectra with S/N between 30 and 60 per resolution element at 5650 Å obtained with the Tull Coudé spectrograph of the 2.7 m telescope at the McDonald Observatory. Although the resolution was not specified in the article, it is presumably $\lambda/\Delta\lambda \sim 60\,000$.

Since our results depend critically on the stellar parameters, we decided to carry out our own spectral analysis. We used the coadded HARPS-N and HARPS spectra, which have an S/N of about 240 at 5650 Å per resolution element and a resolving power of $\lambda/\Delta\lambda = 115\,000$. Our analysis follows the method outlined by Johnson et al. (2016). We used SME version 4.43 (Valenti & Piskunov 1996; Valenti & Fischer 2005) and a grid of the ATLAS12 model atmospheres (Kurucz 2013) to fit spectral features that are sensitive to different photospheric parameters. We adopted the calibration equations of Bruntt et al. (2010) to estimate the microturbulent velocity and fit many isolated and unblended metal lines to determine the projected rotation velocity ($v \sin i$). We derived an effective temperature $T_{\rm eff} = 5470 \pm 30$ K, surface gravity $\log(g) = 4.53 \pm 0.08$ (cgs), and iron content of [Fe/H] $= -0.025 \pm 0.050$ dex. We also derived the abundances of other elements (see Table 3).

We obtained the stellar mass and radius using the PARSEC model isochrones along with the online interface[2] for Bayesian estimation of the stellar parameters from da Silva et al. (2006). For K2-106 we derive a mass of $M_* = 0.945 \pm 0.063\,M_\odot$ and radius of $R_* = 0.869 \pm 0.088\,R_\odot$ (Table 3). These values can be compared with those derived by Adams et al. (2017), who derived $0.93 \pm 0.01\,M_*[M_\odot]$ and $0.83 \pm 0.04\,R_*[R_\odot]$, respectively. Although these values are the same within 1σ, it is interesting to note that values derived by Adams et al. (2017) lead to higher densities for the planets.

---

[2] Available at http://stev.oapd.inaf.it/cgi-bin/param_1.3

We can test and verify the spectroscopic determination using the *Gaia* parallax (3.96 ± 0.78 mas; $d = 253 \pm 50$ pc; Gaia collaboration et al. 2016a,b; Lindegren et al. 2016). The basic idea is that the radius and mass of the star can be determined from the luminosity, $T_{\rm eff}$, and the iron abundance without using the spectroscopic determination of the surface gravity, which is notoriously difficult to measure. The luminosity is derived from the apparent magnitudes and the parallax. An advantage of this method is that the stellar parameters will be determined with a much higher accuracy using forthcoming data from *Gaia*. However, to use this method, we also have to know to which degree the apparent brightness of the star is affected by extinction. Following the method described by Gandolfi et al. (2008), we derived the interstellar extinction $A_{\rm v}$ by fitting the spectral energy distribution of the star to synthetic colors extracted from the NextGen model spectrum with the same photospheric parameters as the star. We find an extinction of $A_{\rm v} = 0.1 \pm 0.1$ mag, as expected given the relatively nearby location (see below) and high galactic latitude of the star. The effect from the extinction is negligible, and we determined the radius and mass of the star using the PARSEC model isochrones. Using this method, we derive a stellar mass of $M_* = 0.902 \pm 0.027\,M_\odot$ and radius of $R_* = 0.882 \pm 0.050\,R_\odot$ (Table 3), which implies a surface gravity of $\log(g) = 4.474 \pm 0.053$ (cgs). The mass and radius of the star derived by this method is again the same within 1σ as our spectroscopic determination and the values derived by Adams et al. (2017).

For the purposes of the present paper, we used our stellar parameter estimates because they are based on spectra with higher resolution and S/N than those used in previous works. However, for completeness, we also give the masses and radii for the two planets derived using stellar parameters from Adams et al. (2017).

3.2. Activity of the host star

Before discussing the RV signals of the planets, we need to know whether stellar activity affects the RV measurements or the light curves. From the HARPS and HARPS-N spectra we derive an average chromospheric activity index $\log R'_{\rm HK} = -5.04 \pm 0.19$ (Table 2). As pointed out by Saar (2006), the minimum chromospheric activity of stars with solar metallicity is about $\log R'_{\rm HK} = -5.08$. Since we do not see any emission component in the Ca II H&K lines (Fig. 1) either, we conclude that the star is very inactive, in agreement with its slow rotation of $v \sin i = 2.8 \pm 0.35$ km s^{-1}. This does not imply, however, that there is no RV jitter caused by stellar activity. Lanza et al. (2016) showed that the amplitude of the long-term RV variation of the Sun in the time from 2006 to 2014 was 4.98 ± 1.44 m s^{-1}. At the maximum of the solar activity, the amplitude of the RV variations can be as high as 8 m s^{-1} (Meunier et al 2010a). The scatter of the RV measurements shown in Figs. 2 and 3 appears to be dominated by the photon noise of the spectra, not by stellar activity, which is consistent with the result that this star is as inactive as the Sun.

Although the orbital periods of the planets are already known from the transit light curve, it is nevertheless useful to perform a period search to investigate whether stellar activity could systematically change the inferred RV amplitudes of the planets, or whether it merely adds random noise to the data. Since the RV variations induced by activity on the Sun are correlated with the $\log R'_{\rm HK}$-index (Meunier et al 2010b), we calculated the Lomb-Scargle diagram for the stellar $\log R'_{\rm HK}$ and the bisector span. The are no significant peaks (false-alarm probability lower
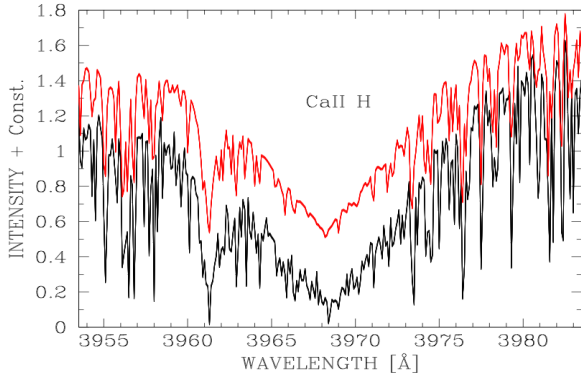
Fig. 1. Averaged HARPS spectrum of K2-106 (black) in the Ca II H line together with a solar spectrum (red).
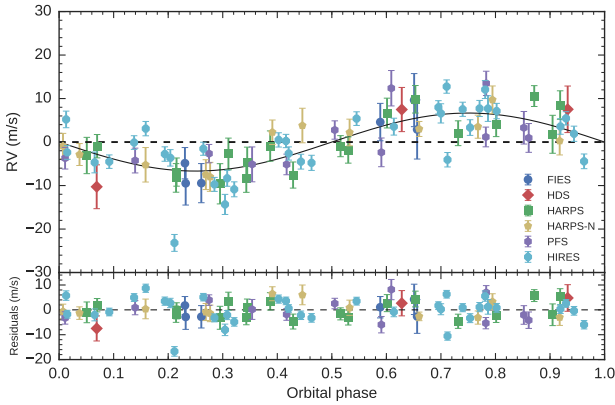

Fig. 2. Phase-folded RV curve of K2-106 b after removing the signal from the outer planet.
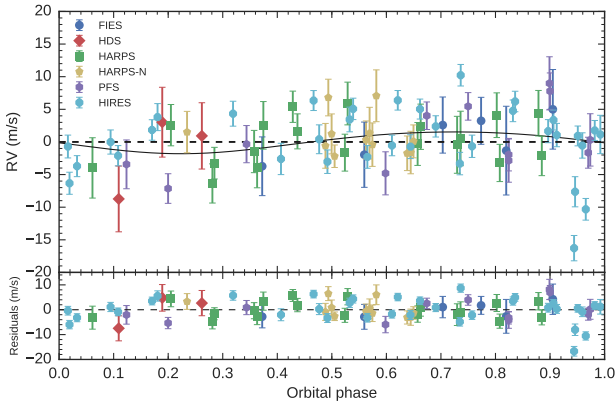

Fig. 3. Phase-folded RV curve of K2-106 c after removing the signal from the inner planet.

than 1%) at the orbital periods of the planets, which means that the observed RV variations are not induced by stellar activity.

In Figs. 4 and 5 we plot $\log R'_{HK}$ and the bisector span against RV. The correlation coefficient between $\log R'_{HK}$ and the RV is -0.07 ± 0.10 and the correlation between the bisector span and the RV is -0.26 ± 0.23. This means that there are no significant correlations between the activity indicators and the RV variations, suggesting that stellar activity does not significantly bias the RV amplitudes (K values). Although the activity of the star is low, we nevertheless include a jitter term in the analysis. The jitter terms and the systemic velocities are given in Tables 1 and 2. However, we also quote the results obtained without using the jitter term, to discuss whether the inclusion of a jitter term makes any significant difference.
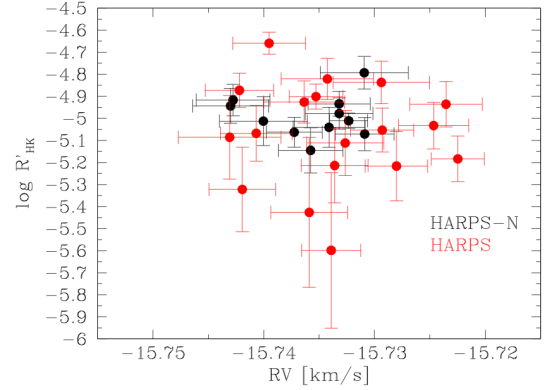
Fig. 4. Same as Fig. 5, but for the chromospheric activity index $\log R'_{HK}$. There is again no correlation between the two.
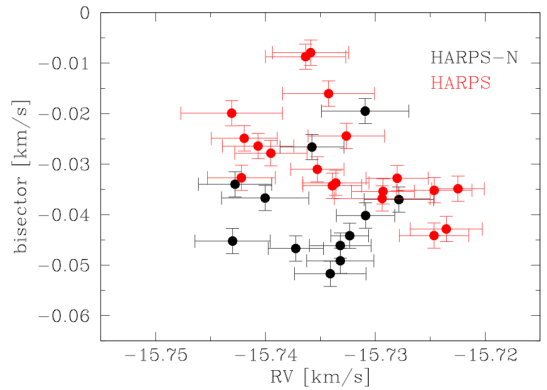

Fig. 5. Bisector span versus the RV for K2-106. There is no correlation between the two, indicating that stellar activity or hypothetical background binaries probably do not affect the derived RV amplitudes for the two planets.

3.3. Multi-planet joint analysis

We performed a joint analysis of the K2 light curve and RV data of K2-106. We used the K2 photometry provided by Vanderburg & Johnson (2014), and detrended and cleaned the transit light curves using the code `exotrending`[3]. For each transit light curve, `exotrending` fits a second-order polynomial to the out-of-transit data. The fitted segments includes 4 and 12 h of out-of-transit data centered around each transit of the inner and outer planet, respectively. The code removes outliers using a 3σ clipping algorithm applied to the residuals to the preliminary best-fitting transit model derived using the equations from Mandel & Agol (2002), coupled to a nonlinear least-squares fitting procedure.

The multi-planet joint analysis was made with the code `pyaneti` (Barragán et al. 2017). This code explores the parameter space with a Markov chain Monte Carlo algorithm and generates a posterior distribution for each parameter. The transit fits are made using a Mandel & Agol (2002) model, while we used Keplerian orbits to model the RV measurements. The likelihood and fitted parameters are the same as in Barragán et al. (2016). For each planet, the fitted parameters are listed in Table 4. Briefly, they are 1) the time of first transit T_0; 2) the orbital period P; 3) $\sqrt{e} \sin \omega_\star$ and 4) $\sqrt{e} \cos \omega_\star$, where e is the eccentricity and $\omega_\star$ is the argument of periapsis of the star; 5) the impact parameter b, defined as $\cos i [1 - e^2]/[R_\star(1 + e \sin \omega_p)]$,

---

Table 4. K2-106 system parameters.

K2-106	
$M_*[M_\odot]$	0.945 ± 0.063
$R_*[R_\odot]$	0.869 ± 0.088
$T_{\rm eff}[K]$	5470 ± 30
Linear limb-darkening coefficient u_1	$0.41^{+0.13}_{-0.12}$
Quadratic limb-darkening coefficient u_2	$0.25^{+0.13}_{-0.12}$
q_1	$0.448^{+0.101}_{-0.096}$
q_2	$0.312^{+0.091}_{-0.089}$

K2-106 b	
T_0 [days]	2457394.0114 ± 0.0010
Period [days]	$0.571292^{+0.000012}_{-0.000013}$
Impact parameter b	$0.18^{+0.19}_{-0.13}$
a/R_*	$2.892^{+0.089}_{-0.135}$
$R_{\rm p}/R_*$	$0.01601^{+0.00031}_{-0.00029}$
Radial velocity semi-amplitude K [m s^{-1}]	6.67 ± 0.69
Orbital eccentricity e	0.0 (fixed)
$\sqrt{e}\sin\omega_\star$	0.0 (fixed)
$\sqrt{e}\cos\omega_\star$	0.0 (fixed)
Inclination i [deg]	$86.4^{+2.5}_{-4.1}$
Orbital semi-major axis a [AU]	0.0116 ± 0.0013
$M_{\rm p}[M_\oplus]$	$8.36^{+0.96}_{-0.94}$
$R_{\rm p}[R_\oplus]$	1.52 ± 0.16
$\rho_{\rm p}[{\rm g\,cm}^{-3}]$	$13.1^{+5.4}_{-3.6}$
$g_{\rm p}[{\rm cm\,s}^{-2}]$	2757^{+369}_{-396}
$T_{\rm eq}^1$ [K]	2333^{+69}_{-57}
τ_{14} [h]	$1.532^{+0.037}_{-0.035}$
$\tau_{12} = \tau_{34}$ [h]	$0.0253^{+0.0037}_{-0.0012}$

K2-106 c	
T_0 [days]	$2457405.73156^{+0.0033}_{-0.0044}$
Period [days]	$13.33970^{+0.00091}_{-0.00096}$
Impact parameter b	$0.31^{+0.17}_{-0.20}$
a/R_*	$26.2^{+2.4}_{-2.7}$
$R_{\rm p}/R_*$	$0.02632^{+0.00075}_{-0.00058}$
Radial velocity semi-amplitude K [m s^{-1}]	$1.67^{+0.99}_{-0.88}$
Orbital eccentricity e	$0.18^{+0.15}_{-0.12}$
ω	178^{+58}_{-74}
$\sqrt{e}\sin\omega_\star$	0.01 ± 0.25
$\sqrt{e}\cos\omega_\star$	$-0.28^{+0.39}_{-0.24}$
Inclination i [deg]	$89.35^{+0.43}_{-0.46}$
Orbital semi-major axis a [AU]	$0.105^{+0.015}_{-0.015}$
$M_{\rm p}[M_\oplus]$	$5.8^{+3.3}_{-3.0}$
$R_{\rm p}[R_\oplus]$	$2.50^{+0.27}_{-0.26}$
$\rho_{\rm p}[{\rm g\,cm}^{-3}]$	$2.0^{+1.6}_{-1.1}$
$g_{\rm p}[{\rm cm\,s}^{-2}]$	843^{+557}_{-447}
$T_{\rm eq}$ [K]	774^{+46}_{-36}
τ_{14} [h]	$3.66^{+0.69}_{-0.57}$

Notes. The variables are explained in Sect. 3.3. The jitter terms and the systemic velocities are given in Tables 1 and 2. $^{(1)}$ Equilibrium temperature $T_{\rm eq}$ derived assuming zero albedo.

where i is the orbital inclination with respect to the line of sight, $R_\star$ is the stellar radius, and $\omega_{\rm p}$ is the argument of periapsis of the planet; 6) the scaled semi-major axis $a/R_\star$; 7) the planet-to-star radius ratio $R_{\rm p}/R_\star$; 8) the RV semi-amplitude variation K; and 9) the systemic velocities γ_j for each instrument j. The code also fits for the limb-darkening coefficients u_1 and u_2 using the parameterization q_1 and q_2 proposed by Kipping et al. (2013). Table 4 reports also the derived quantities, namely, the planetary mass $M_{\rm p}$ and radius $R_{\rm p}$, bulk density $\rho_{\rm p}$, surface grav-

ity $g_{\rm p}$, equilibrium temperature $T_{\rm eq}$ (assuming zero albedo), as well as the transit duration τ_{14} and the ingress/egress duration $\tau_{12} = \tau_{34}$.

The long-cadence data give a slightly distorted view of the actual transit shape. To take this into account, we followed the procedure described by Kipping et al. (2010). We subdivided each time stamp into ten points, calculated the theoretical flux for each point, and then performed an average before comparing to the data. We set uniform priors for the following parameters within the ranges $T_{0,\rm b} = [2\,457\,394.00, 2\,457\,394.02]$ d, $T_{0,\rm c} = [2\,457\,405.69, 2\,457\,405.77]$ d, $P_{\rm b} = [0.5710, 0.5716]$ d, $P_{\rm c} = [13.33, 13.35]$ d, $b_i = [0, 1]$, $K_i = [0, 100]$ m s^{-1}, and $R_{{\rm p},i}/R_\star = [0, 0.1]$. For circular orbits the parameters $\sqrt{e_i}\sin\omega_i$, $\sqrt{e_i}\cos\omega_i$ were fixed to 0, whereas for eccentric orbits the priors for the two eccentricity parameters were uniform between -1 and 1, taking into account that $e < 1$. For the the limb-darkening coefficients u_1 and u_2, we adopted Gaussian priors centered at the values given by Claret & Bloemen (2011) with conservative error bars of 0.1. For the scaled semi-major axis, we used Kepler's third law to set Gaussian priors based on the stellar mass and radius as derived in Sect. 3.1.

The parameter space was explored using 500 independent Markov chains. Once the chains converged to a solution, we ran 25 000 additional iterations with a thin factor of 50. This produced a posterior distribution of 250 000 independent points for each parameter. The final parameters and their corresponding error bars were defined by the median and the 68% levels of the credible interval of the posterior distribution.

Given the very short orbital period, we assumed a circular orbit for K2-106 b, but included eccentricity orbit in the case of K2-106 c. Using the full analysis, all data, and the jitter term, we find $e_{\rm c} = 0.18^{+0.15}_{-0.12}$ for K2-106 c. Figure 3 shows the phase-folded RV curve and the orbit with an eccentricity of 0.18.

There are in principle four possibilities for obtaining the mass of the two planets: we can use just our data, or we can also include the data taken by Sinukoff et al. (2017b), and we can perform the analysis with and without the jitter term. The K-amplitudes using our data without the jitter term are $K_{\rm b} = 6.25 \pm 0.63$ m s^{-1} and $K_{\rm c} = 2.38 \pm 0.80$ m s^{-1}. With the jitter terms they are $K_{\rm b} = 6.39 \pm 0.85$ m s^{-1}, and $K_{\rm c} = 1.76 \pm 1.0$ m s^{-1}. The effect of the jitter term is thus small, as these values are the same within 1σ. When we include the measurements taken by Sinukoff et al. (2017b) and the jitter term, we find $K_{\rm b} = 6.67 \pm 0.69$ m s^{-1}, $K_{\rm c} = 1.67^{+0.99}_{-0.88}$ m s^{-1}. The inclusion of a jitter term and the data from Sinukoff et al. (2017b) thus does not change the results significantly, but the accuracy of the mass determination increases slightly when we include the data from Sinukoff et al. (2017b). In the following we use the values obtained with the jitter term and including the data taken by Sinukoff et al. (2017b).

Using the masses and orbital parameters of the two planets, we estimated the expected transit-time-variations (TTVs) induced by the gravitational mutual interactions between the two objects. Because the two planets are not in resonance, the interaction between the two planets is very small. The resulting TTVs are too small to be detected using *Kepler* long-cadence data.

3.4. Radii, masses, and densities of the planets

The phase-folded RV curves of K2-106 b and K2-106 c are shown in Figs. 2 and 3. Figures 6 and 7 show the phase-folded transit light curves. When we use the data obtained by Sinukoff et al. (2017b), the jitter terms, and the stellar parameters derived by us, the masses of the two planets are $M_{\rm b} = 8.36^{+0.96}_{-0.94}\,M_\oplus$, and $M_{\rm c} = 5.8^{+3.3}_{-3.0}\,M_\oplus$ outer planet, respectively. The radius of
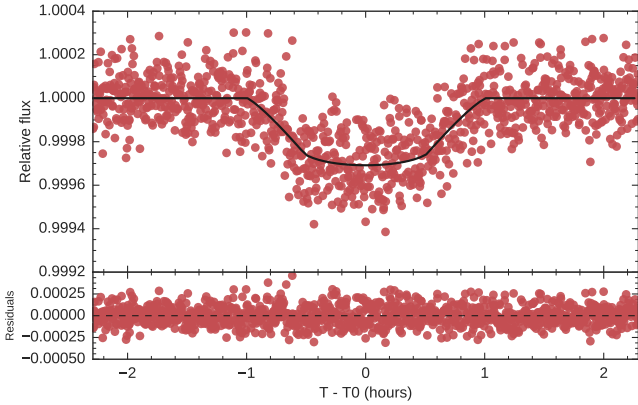
Fig. 6. Best-fit light curves of the planet K2-106 b. The light curve has been folded using the orbital period of the planet (Table 4).
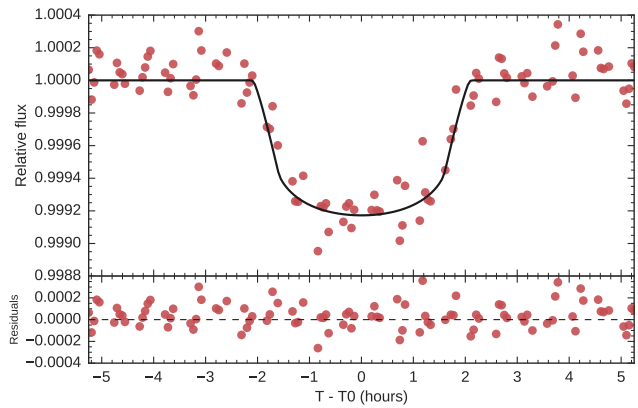

Fig. 7. Best-fit light curves to planet K2-106 c. The light curve has been folded using the orbital period of the planet (Table 4).

inner planet is $R_b = 1.52 \pm 0.16\,R_\oplus$, and $R_c = 2.50^{+0.27}_{-0.26}\,R_\oplus$ for the outer planet. With these values, the mean densities are $13.1^{+5.4}_{-3.6}\,\mathrm{g\,cm^{-3}}$ and $2.0^{+1.6}_{-1.1}\,\mathrm{g\,cm^{-3}}$ for the two planets, respectively. All the values derived for the two planets are listed in Table 4. The radii we have derived are consistent with the values of $R_p = 1.46 \pm 0.14\,R_\oplus$ and $R_p = 2.53 \pm 0.14\,R_\oplus$ for the two planets given by Adams et al. (2017).

With the stellar parameters given in Adams et al. (2017), the mass and radius of the inner planet becomes $M_b = 8.22^{+0.94}_{-0.92}\,M_\oplus$, and $R_b = 1.45 \pm 0.15\,R_\oplus$, respectively. With these values the density increases to $\rho_b = 14.8^{+6.1}_{-4.0}\,\mathrm{g\,cm^{-3}}$. For the outer planet, we find $M_c = 5.7^{+3.3}_{-3.0}\,M_\oplus$, and $R_c = 2.39 \pm 0.25\,R_\oplus$, respectively.

3.5. Atmospheric escape rates

Because of the relatively similar masses of the planets and their differing orbital distances, K2-106 is an excellent laboratory for the study of atmospheric escape. K2-106 b adds to the sample of ultra-short period planets, such as CoRoT-7b (Léger et al. 2009) and Kepler-10b (Batalha et al. 2011), for which the bulk density is suggestive of an Earth-like composition. Such ultra-short period planets have a Jeans escape parameter Λ below ≈ 20. This is also the case for K2-106b, which has $\Lambda = 17.1 \pm 2.6$.

As mentioned in the introduction, the atmosphere of planets with Λ values lower than 20−40, depending on the system parameters, lie in the boil-off regime (Owen & Wu 2016; Cubillos et al. 2017), where the escape is driven by the atmospheric thermal energy and low planetary gravity, rather than the high-energy (XUV) stellar flux. Fossati et al. (2017) showed that the hydrogen-dominated atmosphere of planets with an equilibrium temperature higher than 1000 K, a mass lower than about $5\,M_\oplus$, and a Λ value lower than 20−40 should evaporate completely in less than about 500 Myr. As indicated by these theoretical results and by the planet's high bulk density, K2-106 b has probably lost any hydrogen-dominated atmosphere it may once have had. Because of the very close distance to the host star, the planet has probably also lost any secondary, likely CO_2-dominated, atmosphere because of the intense stellar radiation (Kulikov et al. 2006; Tian 2009). The planet could therefore have been left with a bare rocky surface exposed to the intense stellar radiation and wind. This may have led to the formation of surface magma oceans (Leger et al. 2011; Miguel et al. 2011; Demory et al. 2016) that outgas and sputter, in a way similar from what occurs on Mercury (Pfleger et al. 2015). This could create an extended escaping exosphere composed mostly of heavy refractory elements (Mura et al. 2011).

The parameters of K2-106 c are nearly identical to those of Kepler 454 b (Gettel et al. 2016). Kepler 454 b is the innermost known planet of a system that also has a massive planet with an orbital period of 527 d. Whether planets like K2-106 c and Kepler 454 b have a rocky core and an extended atmosphere or if they belong to the elusive class of "ocean planets" (Léger et al. 2004) cannot be deduced from the mass and radius measurements alone. Further studies are needed to clarify the situation, but, as mentioned above, it is reasonable to assume that K2-106 c has a rocky core and an extended atmosphere.

The status and evolution of the atmosphere of K2-106 c is also less certain because of the rather large uncertainty in the planet's mass. We estimated the XUV-driven escape rate based on the energy-limited formulation of Erkaev et al. (2007) and an XUV (XUV: 1–912 Å) flux rescaled from the solar flux (since the star has a solar-like activity level), obtaining a mass-loss rate M_{en} of $2 \times 10^9\,\mathrm{g\,s^{-1}}$. We also employed the hydrodynamic upper-atmosphere code described by Erkaev et al. (2016), obtaining a mass-loss rate M_{hy} of $4 \times 10^9\,\mathrm{g\,s^{-1}}$. This and the fact that the planet's Λ value is 25.8 ± 9.2 suggest that the planetary atmosphere may be in the boil-off regime (Owen & Wu 2016; Fossati et al. 2017). The parameters relevant to atmospheric escape are listed in Table 5.

We now assume that the atmosphere of K2-106 c is hydrogen dominated, as suggested by the low bulk density, and that it is indeed in the boil-off regime. This would imply that the atmosphere would almost completely escape within a few hundred Myr (Fossati et al. 2017), which is not compatible with the measured bulk density and age of the system, which is certainly older than a few a few hundred Myr. It is also extremely unlikely that we have observed the planet during a short-lived transition phase characterized by an extremely high escape rate. Under the current assumptions, the most likely possibility is that either the radius and/or equilibrium temperature are overestimated and/or the mass is underestimated (Cubillos et al. 2017). This is the same situation as considered by Lammer et al. (2016) for CoRoT-24 b (Alonso et al. 2014) and then extended by Cubillos et al. (2017) to a large sample of low-density sub-Neptune-mass planets. These authors showed that a radius overestimation may be caused by the presence of high-altitude clouds. At the same time, the presence of clouds would also imply that the equilibrium temperature may have been overestimated because this would increase the albedo (see Cubillos et al. 2017, for more details). A better understanding of the loss processes would be possible with a higher accuracy in the mass and radius determinations of the planet and the star.

Table 5. Atmospheric escape parameters.

K2-106 b	
Restricted Jeans escape parameter Λ	17.1 ± 2.6
Roche-lobe radius [$R_\oplus$]	4
F_{XUV} [erg cm^{-2} s^{-1}]	11 500
Escape rate [s^{-1}]	$2.1 \times 10^{+33}$
$F_p/F_\oplus^1$	3500
K2-106 c	
Restricted Jeans escape parameter Λ	25.8 ± 9.2
Roche-lobe radius [$R_\oplus$]	33
F_{XUV} [erg cm^{-2} s^{-1}]	154
Escape rate [s^{-1}]	$6.6 \times 10^{+31}$
$F_p/F_\oplus^1$	52

Notes. [1] Ratio of the stellar flux received by the planet compared to Earth.

4. Discussion and conclusions

We have determined the masses of the planets K2-106 b and K2-106 c. K2-106 b is a low-mass ultra-short-period planet. Table 6 gives an overview of the known planets of this type. Other planets of this class are CoRoT-7b (Léger et al. 2009), 55 Cnc e (Winn et al. 2011), Kepler-10b (Batalha et al. 2011), Kepler-78b (Sanchis-Ojeda et al. 2013), WASP-47e (Dai et al. 2015; Sinukoff et al. 2017a), and perhaps also the planet candidates of the sdB KIC 05807616 (Charpinet et al. 2011). Because KOI 1843.03 has an orbital period of only 4.425 h, Rappaport et al. (2013) concluded that this planet must have a density higher than $\rho = 7$ g cm^{-3}. Adams et al. (2016) recently published a list of 19 additional planet candidates with orbital periods shorter than one day. One of these is EPIC 203533312, which has an orbital period of 4.22 h. If confirmed as a planet, its density must be higher than $\rho = 8.9$ g cm^{-3}.

The upper panel in Fig. 8 shows the mass-radius relation for low-mass ultra-short planets together with various compositions taken from Zeng et al. (2016). The filled red symbols are the values for K2-106 b and K2-106 c using our stellar parameters, the open symbol those for the stellar parameters given by Adams et al. (2017). In both cases, K2-106 b is located between the lines with 50% and 100% iron composition. How robust is this conclusion that K2-106 b is metal rich? When we use models published by Fortney et al. (2007) or Wurm et al. (2013), we obtain the same results. Thus, regardless of which set of stellar parameters we use, whether we include the jitter term, and regardless of which models we use, in all cases we reach the conclusion that the iron core contains more than half of the mass of the planet. The conclusion that this planet is metal rich is therefore robust. In order to constrain the composition more precisely, we used our own planetary models. These are two-layer models of iron and silicates (MgSiO$_3$) based on the model of Wagner (2011). Using these models, we find that an iron core contains $80^{+20}_{-30}\%$ of the mass of the planet. The composition is Mercury-like rather than Earth-like. This is very interesting because other ultra-short planets seem to have an Earth-like composition. The high metal content of the planet is particularly surprising because the host star has solar metallicity (Table 3). The unusual composition of K2-106 b also shows that rocky planets are more diverse than previously thought, and it can provide important clues of how such metal-rich planets form.

As pointed out by Alessi et al. (2017), the variety of chemical compositions observed for giant planets could be caused by variations in metallicities of their host stars or by the accretion of material at different locations in disks around stars with similar
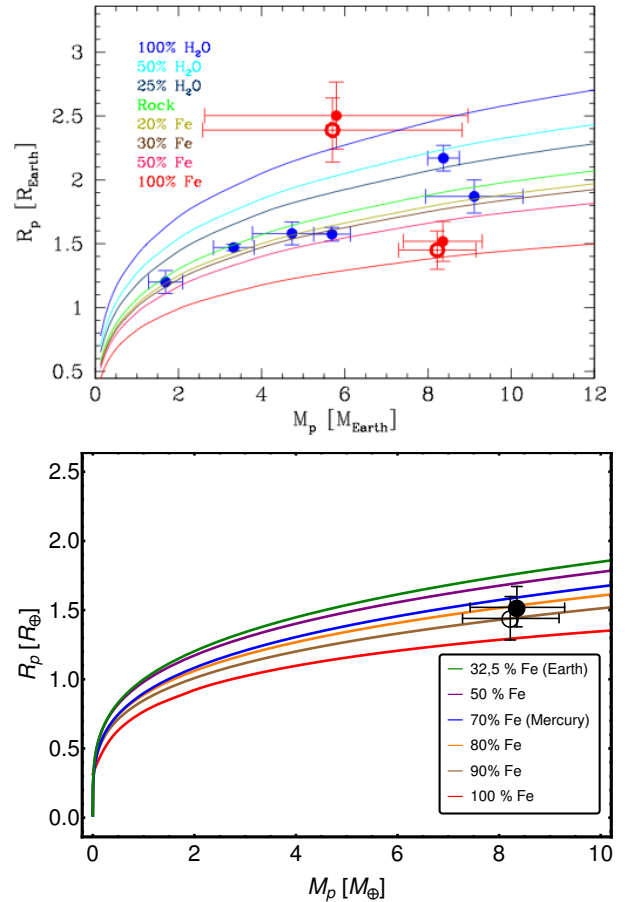
Fig. 8. *Upper panel*: mass-radius relation for low-mass ultra-short planets. K2-106 b, c are the red filled symbols obtained using the stellar parameters derived by us. The open red symbol shows the same, but for the parameters given by Adams et al. (2017). The blue symbols are all other known ultra-short period planets. *Lower panel*: detailed position of K2-106 b, c using models calculated by us. The iron core contains about 80% of the mass of the planet.

compositions. Thorngren et al. (2016) have studied the relation between the planetary heavy-element mass and the total planet mass for planets in the mass range between 20 and 3000 $M_\oplus$ (0.07−10 M_{Jup}). They found a clear correlation between the two, in the sense that heavy-element mass increases with the mass of the host star.

Measuring abundances for low-mass ultra-short period planets is particularly interesting because the densities of planets without atmospheres constrain the formation of planets (Raymond et al. 2013). For example, close-in planets with a high water content are likely to have formed at a larger distance from the host star and then migrated inward. An interesting result emerging from the models calculated by Lopez (2017) is that planets that receive around 2800 times the stellar flux of Earth can keep substantial water envelopes. Such planets would have $R_p \geq 2 R_\oplus$. This is not the case for K2-106 b, which means that it must have formed from water-poor material inside the snow line.

When we apply the same logical argument to the iron versus silicate contents, it would mean that K2-106 b formed from metal-rich material. In the solar system, Mercury is 70% metal and 30% silicate, which implies a similar formation scenario as for K2-106 b. Therefore it is reasonable to consider similar formation scenarios for K2-106 b and Mercury. In this respect, it is

Table 6. Low-mass ultra-short-period planets with known densities.

Planet	Orbital period [d]	Mass [$M_\oplus$]	Radius [$R_\oplus$]	Density [$\mathrm{g\,cm^{-3}}$]	Multiple system[1]	Ref.
KOI 1843.03	0.18	$\geq 0.46^3$	$0.45^{+0.08}_{-0.05}$	$\geq 7^3$	NO	Rappaport et al. (2013)
Kepler-78 b	0.36	1.69 ± 0.41	1.20 ± 0.09	5.3 ± 1.8	NO	Howard et al. (2013)
K2-106 b	0.57	$8.36^{+0.96}_{-0.94}$	1.52 ± 0.16	$13.1^{+5.4}_{-3.6}$	YES	this work
55 Cnc e[2]	0.74	8.63 ± 0.35	2.00 ± 0.14	$5.9^{+1.5}_{-1.1}$	YES	Winn et al. (2011)
55 Cnc e[2]	0.74	8.37 ± 0.38	2.17 ± 0.10	4.5 ± 0.20	YES	Winn et al. (2012)
WASP-47 e[2]	0.79	12.2 ± 3.7	1.817 ± 0.065	11.3 ± 3.6	YES	Dai et al. (2015)
WASP-47 e[2]	0.79	9.11 ± 1.17	1.87 ± 0.13	7.63 ± 1.90	YES	Sinukoff et al. (2017a)
Kepler-10 b	0.84	3.33 ± 0.49	$1.47^{+0.03}_{-0.02}$	5.8 ± 0.8	YES	Dumusque et al. (2014)
CoRoT-7 b	0.85	4.73 ± 0.95	1.58 ± 0.09	6.61 ± 1.72	YES	Haywood et al. (2014)
HD3167 b	0.95	5.69 ± 0.44	1.574 ± 0.054	$8.00^{+1.10}_{-0.98}$	YES	Gandolfi et al. (2017)

Notes. [1] "NO" means that no other planet is known. [2] Two measurements were obtained for this planet. [3] Lower limit of mass and density estimated from orbital period and radius.

interesting to note that Wurm et al. (2013) argued that the high iron abundance of Mercury is due to the photophoresis in the protoplanetary disk and not the result of a giant impact, as was previously thought. Photophoresis is a process in which iron and silicates are separated in the disk. Iron ends up in the very innermost part of the disk, with silicates at somewhat larger distances. At the current location, the temperature is also higher than the silicate evaporation temperature in the disk, which is in the range between 1300 and 1450 K (Gail 1998). Is it possible that ultra-short period planets form close to the star from iron-rich material? A planet of 8 $M_\oplus$, forming at 0.012 AU, certainly requires much material in the disk, but according to the model published by Hasegawa & Pudritz (2013), it is possible to form such planets close to the star. If ultra-short period planets are forming close to the star, many of them should be iron-rich. Clearly, more research in this field is needed, but the results so far obtained show that studies of ultra-short period planets can give us key information on how and where low-mass planets form.

Another interesting aspect of the K2-106 b,c system is that the masses of the two planets are relatively similar, but the densities are very different. Since the mass and radius measurements for both planets are affected in the same way by the systematic uncertainties of the stellar parameters, the diversity of exoplanets (e.g., Hatzes & Rauer 2015) cannot be entirely explained by problems in the determination of the stellar parameters. As shown in Fig. 8, the density of K2-106 c is consistent with a planet composed of 50% rock and 50% ice. However, as pointed out above, other planets like this one consist of a rocky core with a hydrogen atmosphere (Chen et al. 2017). Since the mass is $M_c = 5.8^{+3.3}_{-3.0}\ M_\oplus$ and the ratio of the stellar flux received by the planet compared to Earth is $F_p/F_\oplus \sim 52$, there is no reason why it could not have a hydrogen atmosphere since at about 800 K a 50% ice content is not very plausible. The difference in atmospheric loss rates, which we have discussed in Sect. 3.5, explains why the inner planet has no hydrogen atmosphere, while the other planet is likely to have one. However, as we pointed out above, the fact that Λ is in the interesting regime between 20 and 40 makes K2-106 c an ideal target for future studies of atmospheric escape, particularly because the host star is much brighter than that of CoRoT-24 b (Alonso et al. 2014).

We conclude that K2-106 (EPIC 220674823, TYC 608-458-1) is an interesting system that deserves further study. The accuracy with which the radius of the star and thus also the planets can be determined will increase once

Gaia collects more data. A logical step for future work is to search for the extended escaping exosphere atmosphere of K2-106 b that has been suggested by Mura et al. (2011) by obtaining spectroscopic transit observations in a similar way as for CoRoT-7b (Guenther et al. 2011).

References

Adams, E. R., Jackson, B., & Endl, M. 2016, AJ, 152, 47
Adams, E. R., Jackson, B., & Endl, M., et al. 2017, AJ, 153, 82
Alessi, M., Pudritz, R. E., & Cridland, A. J. 2017, MNRAS, 464, 428
Alonso, R., Moutou, C., Endl, M., et al. 2014, A&A, 567, A112
Baranne, A., Queloz, D., Mayor, M., et al. 1996, A&AS, 119, 373
Barragán, O., Grziwa, S., Gandolfi, D., et al. 2016, AJ, 152, 193
Barragán, O., Gandolfi, D., & Antoniciello, G. 2017, Astrophysics Source Code Library [record ascl:1707.003]

Batalha, N. M., Borucki, W. J., Bryson, S. T., et al. 2011, ApJ, 729, 27
Berta-Thompson, Z. K., Irwin, J., Charbonneau, D., et al. 2015, Nature, 527, 204
Bourrier, V., Lecavelier des Etangs, A., Ehrenreich, D., Tanaka, Y. A., & Vidotto, A. A. 2016, A&A, 591, A121
Bruntt, H., Bedding, T. R., Quirion, P.-O., et al. 2010, MNRAS, 405, 1907
Butler, R. P., Marcy, G. W., Williams, E., et al. 1996, PASP, 108, 500
Carter, J. A., Agol, E., Chaplin, W. J., et al. 2012, Science, 337, 556
Charpinet, S., Fontaine, G., Brassard, P., et al. 2011, Nature, 480, 496
Chen, G., Guenther, E. W., Palle, E., et al. 2017, A&A, 600, A138
Claret, A., & Bloemen, S. 2011, A&A, 529, A75
Cosentino, R., Lovis, C., Pepe, F., et al. 2012, Proc. SPIE, 8446, 84461
Crane, J. D., Shectman, S. A., Butler, R. P., et al. 2006, Proc. SPIE, 7735, 773553
Crane, J. D., Shectman, S. A., Butler, R. P., Thompson, I. B., & Burley, G. S. 2008, Proc. SPIE, 7014, 701479
Crane, J. D., Shectman, S. A., & Butler, R. P. 2010, Proc. SPIE, 6269, 626931
Cubillos, P., Erkaev, N. V., Juvan, I., et al. 2017, MNRAS, 466, 1868
Dai, F., Winn, J. N., Arriagada, P., et al. 2015, ApJ, 813, L9
da Silva, L., Girardi, L., Pasquini, L., et al. 2006, A&A, 458, 609
Demory, B.-O., Gillon, M., de Wit, J., et al. 2016, Nature, 532, 207
Dressing, C. D., Charbonneau, D., Dumusque, X., et al. 2015, ApJ, 800, 135
Dumusque, X., Bonomo, A. S., Haywood, R. D., et al. 2014, ApJ, 789, 154
Ehrenreich, D., Bourrier, V., Wheatley, P. J., et al. 2015, Nature, 522, 459
Eigmüller, P., Gandolfi, D., Persson, C. M., et al. 2017, AJ, 153, 130
Endl, M., Robertson, P., Cochran, W. D., et al. 2012, ApJ, 759, 19
Erkaev, N. V., Kulikov, Y. N., Lammer, H., et al. 2007, A&A, 472, 329
Fortney, J. J., Marley, M. S., & Barnes, J. W. 2007, ApJ, 659, 1661
Fossati, L., Erkaev, N. V., Lammer, H., et al. 2017, A&A, 598, A90
Frandsen, S., & Lindberg, B. 1999, in Astrophysics with the NOT, Proceedings, eds. H. Karttunen, & V. Piirola, Anot. Conf., 71
Gaia Collaboration (Brown, A. G. A., et al.) 2016a, A&A, 595, A2
Gaia Collaboration (Prusti, T., et al.) 2016b, A&A, 595, A1
Gail, H.-P. 1998, A&A, 332, 1099
Gandolfi, D., Alcalá, J. M., Leccia, S., et al. 2008, ApJ, 687, 1303
Gandolfi, D., Parvianinen, H., Deeg, H. J., et al. 2015, A&A, 576, A11
Gandolfi, D., Barragán, O., Hatzes, A. P., et al. 2017, AJ, 154, 123
Gettel, S., Charbonneau, D., Dressing, C. D., et al. 2016, ApJ, 816, 95
Girardi, L., Bertelli, G., Bressan, A., et al. 2000, A&A, 391, 195
Girardi, L., Bressan, A., Bertelli, G., & Chiosi, C. 2002, A&AS, 141, 371
Guenther, E. W., Cabrera, J., Erikson, A., et al. 2011, A&A, 525, A24
Hasegawa, Y., & Pudritz, R. E. 2013, ApJ, 778, 78
Hatzes, A. P., & Rauer, H. 2015, ApJ, 810, L25
Haywood, R. D., Collier Cameron, A., Queloz, D., et al. 2014, MNRAS, 443, 2517
Howard, A. W., Sanchis-Ojeda, R., Marcy, G. W., et al. 2013, Nature, 503, 381
Huber, D., Bryson, S. T., Haas, M. R., et al. 2016, ApJS, 224, 2
Johnson, M. C., Gandolfi, D., Fridlund, M., et al. 2016, AJ, 151, 171
Kipping, D. M. 2010, MNRAS, 408, 1758
Kipping, D. M. 2013, MNRAS, 435, 2152
Kulikov, Y. N., Lammer, H., Lichtenegger, H. I. M., et al. 2006, P&SS, 54, 1425
Kurucz, R. L. 2013, ATLAS12: Opacity sampling model atmosphere program, Astrophysics Source Code Library
Lammer, H., Stökl, A., Erkaev, N. V., et al. 2014, MNRAS, 439, 3225
Lammer, H., Erkaev, N. V., Fossati, L., et al. 2016, MNRAS, 461, L62
Lanza, A. F., Molaro, P., Monaco, L., & Haywood, R. D. 2016, A&A, 587, A103
Léger, A., Selsis, F., Sotin, C., et al. 2004, Icarus, 169, 499
Léger, A., Rouan, D., Schneider, J., et al. 2009, A&A, 506, 287
Léger, A., Grasset, O., Fegley, B., et al. 2011, Icarus, 213, 1
Lindegren, S., Codella, C., Cobrit, S., et al. 2016, A&A, 595, A4
Lopez, E. D. 2017, MNRAS, 472, 245
Lundkvist, M. S., Kjeldsen, H., Albrecht, S., et al. 2016, Nat. Comm., 7, 11201
Mandel, K., & Agol, E. 2002, ApJ, 580, L171
Mayor, M., Pepe, F., Queloz, D., et al. 2003, The Messenger, 114, 20
Meunier, N., Lagrange, A.-M., & Desort, M. 2010a, A&A, 519, A66
Meunier, N., Desort, M., & Lagrange, A.-M. 2010b, A&A, 512, A39
Miguel, Y., Kaltenegger, L., Fegley, B., & Schaefer, L. 2011, ApJ, 742, L19
Motalebi, F., Udry, S., Gillon, M., et al. 2015, A&A, 584, A72
Mura, A., Wurz, P., Schneider, J., et al. 2011, Icarus, 211, 1
Narita, N., Hirano, T., Fukui, A., et al. 2017, PASJ, 69, 29
Noguchi, K., Aoki, W., Kawanomoto, S., et al. 2002, PASJ, 54, 855
Owen, J. E., & Wu, Y. 2016, ApJ, 817, 107
Pepe, F., Mayor, M., Galland, F., et al. 2002, A&A, 388, 632
Pfleger, M., Lichtenegger, H. I. M., Wurz, P., et al. 2015, P&SS, 115, 90
Rappaport, S., Sanchis-Ojeda, R., Rogers, L. A., Levine, A., & Winn, J. N. 2013, ApJ, 773, L15
Raymond, S. N., Barnes, R., & Mandell, A. M. 2008, MNRAS, 384, 663
Saar, S. H. 2006, in AAS/Solar Physics Division Meeting 37, BAAS, 38, 240
Sanchis-Ojeda, R., Rappaport, S., Winn, J. N., et al. 2013, ApJ, 774, 54
Sanchis-Ojeda, R., Rappaport, S., Winn, J. N., et al. 2014, ApJ, 787, 47
Sato, B., Kambe, E., Takeda, Y., Izuminre, H., & Ando, H. 2002, PASJ, 54, 873
Sinukoff, E., Howard, A. W., Petigura, E. A., et al. 2017a, AJ, 153, 70
Sinukoff, E., Howard, A. W., Petigura, E. A., et al. 2017b, AJ, 153, 271
Tajitsu, A., Aoki, W., & Yamamuro, T. 2012, PASJ, 64, 77
Telting, J. H., Avila, G., Buchhave, L., et al. 2014, Astron. Nachr., 335, 41
Thorngren, D. P., Fortney, J. J., Murray-Clay, R. A., & Lopez, E. D. 2016, ApJ, 831, 64
Tian, F. 2009, ApJ, 703, 905
Valenti, J. A., & Fischer, D. A. 2005, ApJS, 159, 141
Valenti, J. A., & Piskunov, N. 1996, A&AS, 118, 595
Vanderburg, A., & Johnson, J. A. 2014, PASP, 126, 948
Vanderburg, A., Latham, D. W., Buchhave, L. A., et al. 2016, ApJS, 222, 14
Wagner, F. W., Sohl, F., Hussmann, H., Grott, M., & Rauer, H. 2011, Icarus, 214, 366
Winn, J. N., Matthews, J. M., Dawson, R. I., et al. 2011, ApJ, 737, L18
Wurm, G., Trieloff, M., & Rauer, H. 2013, ApJ, 769, 78
Zeng, L., Sasselov, D. D., & Jacobsen, S. B. 2016, ApJ, 819, 127

1 Thüringer Landessternwarte Tautenburg, Sternwarte 5, 07778 Tautenburg, Germany
  e-mail: guenther@tls-tautenburg.de
2 Dipartimento di Fisica, Universitá di Torino, via P. Giuria 1, 10125 Torino, Italy
3 Department of Physics and Kavli Institute for Astrophysics and Space Research, Massachusetts Institute of Technology, Cambridge, MA 02139, USA
4 Department of Earth and Planetary Sciences, Tokyo Institute of Technology, 2-12-1 Ookayama, Meguro-ku, 152-8551 Tokyo, Japan
5 Leiden Observatory, Leiden University, 2333CA Leiden, The Netherlands
6 Department of Space, Earth and Environment, Chalmers University of Technology, Onsala Space Observatory, 439 92 Onsala, Sweden
7 Instituto de Astrofísica de Canarias (IAC), 38205 La Laguna, Tenerife, Spain
8 Space Research Institute, Austrian Academy of Sciences, Schmiedlstrasse 6, 8042 Graz, Austria
9 Institute for Computational Science, Center for Theoretical Astrophysics & Cosmology, University of Zurich, Winterthurerstr. 190, 8057 Zurich, Switzerland
10 Rheinisches Institut für Umweltforschung an der Universität zu Köln, Aachener Strasse 209, 50931 Köln, Germany
11 Departamento de Astrofísica, Universidad de La Laguna (ULL), 38206 La Laguna, Tenerife, Spain
12 Stellar Astrophysics Centre, Department of Physics and Astronomy, Aarhus University, Ny Munkegade 120, 8000 Aarhus C, Denmark
13 Institute of Planetary Research, German Aerospace Center, Rutherfordstrasse 2, 12489 Berlin, Germany
14 Center for Astronomy and Astrophysics, TU Berlin, Hardenbergstr. 36, 10623 Berlin, Germany
15 Department of Astronomy, The University of Tokyo, 7-3-1 Hongo, Bunkyo-ku, 113-0033 Tokyo, Japan
16 Astrobiology Center, NINS, 2-21-1 Osawa, Mitaka, 181-8588 Tokyo, Japan
17 National Astronomical Observatory of Japan, NINS, 2-21-1 Osawa, Mitaka, 181-8588 Tokyo, Japan
18 Carnegie Institution of Washington, Department of Terrestrial Magnetism, 5241 Broad Branch Road, NW, Washington, DC 20015-1305, USA
19 Department of Astronomy and McDonald Observatory, University of Texas at Austin, 2515 Speedway, Stop C1400, Austin, TX 78712, USA
20 The Observatories of the Carnegie Institution of Washington, 813 Santa Barbara Street, Pasadena, CA 91101, USA
21 Harvard-Smithsonian Center for Astrophysics, 60 Garden Street, Cambridge, MA 02138, USA
22 Princeton University, Department of Astrophysical Sciences, 4 Ivy Lane, Princeton, NJ 08540, USA
23 University of Southern Queensland, Computational Science and Engineering Research Centre, Toowoomba QLD 4350, Australia